


Nanoscale polar regions embedded within ferroelectric domains in $\text{Na}_{1/2}\text{Bi}_{1/2}\text{TiO}_3\text{-BaTiO}_3$

Ann-Katrin Fetzter ^{*}, Andreas Wohninsland , K. V. Lalitha , and Hans-Joachim Kleebe 
Department of Materials and Earth Sciences, Technical University of Darmstadt, D-64287 Darmstadt, Germany

 (Received 21 December 2021; accepted 16 May 2022; published 17 June 2022)

Relaxor ferroelectrics are an eminent group of functional materials, characterized by complex micro- and nanoscale structures, accounting for their enhanced piezoelectric properties. In the $(1-x)\text{Na}_{1/2}\text{Bi}_{1/2}\text{TiO}_3\text{-}x\text{BaTiO}_3$ (NBT-BT) solid solution, the evolution of nanoscale domains and their hierarchical association with ferroelectric domains is investigated using conventional and scanning transmission electron microscopy on compositions with 6, 9, and 12 mol % BT. Short-range fluctuations in the local polar displacement (polar nanoregions, PNRs) account for a heterogeneous nanostructure at the morphotropic phase boundary (6 mol % BT). Platelike nanodomains of tetragonal $P4bm$ symmetry coexist with a minor volume fraction of rhombohedral $R3c$ nanodomains. Their overall population decreases with increasing BT content. However, ferroelectric $P4mm$ domains in the composition with 12 mol % BT still exhibit nanoscale regions, which deviate from the average polarization. Small volume fractions of both $P4bm$ and $R3c$ nanodomains remain embedded within the ferroelectric domains. This hierarchical domain configuration underpins the complex structural characteristics of NBT-based relaxor ferroelectrics.

DOI: [10.1103/PhysRevMaterials.6.064409](https://doi.org/10.1103/PhysRevMaterials.6.064409)

I. INTRODUCTION

Relaxor ferroelectrics find wide applications ranging from sensor and actuator technologies to energy conversion in transducers. Those with a disordered perovskite structure comprise short-ranged polarized regions, whose dynamic response allows for high permittivities, diffuse phase transitions, and large electrostriction [1]. Among lead-free ceramics, $\text{Na}_{1/2}\text{Bi}_{1/2}\text{TiO}_3$ (NBT)-based compositions show high potential for piezoelectric high-power applications [2–4]. The solid solution $(1-x)\text{Na}_{1/2}\text{Bi}_{1/2}\text{TiO}_3\text{-}x\text{BaTiO}_3$ (NBT-BT) has been widely studied due to enhanced piezoelectric properties at its morphotropic phase boundary (MPB). Relaxor ferroelectric NBT exhibits local A -site chemical and displacive disorder, resulting in a complex structure, described with a rhombohedral ($R3c$) and/or monoclinic (Cc) symmetry [5–8]. Nanometer-sized platelets of tetragonal (T) $P4bm$ symmetry were observed within the $R3c$ matrix [9]. In contrast, the end member BaTiO_3 (BT) is a classical ferroelectric of tetragonal $P4mm$ symmetry, displaying a long-range lamellar ferroelectric domain structure [10,11]. The NBT-BT system is rhombohedral (R) until the MPB with $x \approx 0.05\text{--}0.07$, where R ($R3c$) and T ($P4bm$) phases coexist [12–15]. Both phases display superlattice reflections (SR) in electron diffraction patterns due to tilting of the oxygen octahedra [15,16]. The $P4bm$ phase comprises an $a^0a^0c^+$ oxygen octahedral tilting, resulting in SR of the type $\frac{1}{2}\{ooe\}$ (“ o ” for odd and “ e ” for even Miller indices). The $R3c$ phase can be allocated to the $a^-a^-a^-$ antiphase tilt system, featuring SR of the type $\frac{1}{2}\{ooo\}$. The phase mixture at the MPB is described as volumes of larger $R3c$ domains adjacent to $P4bm$ nanodomains [17]. The MPB composition $x = 0.06$ (NBT-6BT) is often associated with an average pseudocubic structure [18,19], since the rhombohedral and tetragonal phases feature very small distortions from

the cubic symmetry. The $P4bm$ phase was observed in a large compositional range of $0.05 < x < 0.11$ [12]. For $x > 0.11$, the system is described as ferroelectric with $P4mm$ symmetry [20], where oxygen octahedral tilting is absent. Both nanodomains and lamellar domains were observed, however, only in different grain regions [17]. A recent study reports on the coexistence of both tetragonal phases ($P4bm + P4mm$) over a larger compositional range of $0.065 < x < 0.18$ [13].

The relaxor nature of NBT-6BT reflects in a frequency dispersion of the temperature-dependent permittivity response [21]. Relaxor characteristics are influenced by the existence of short-range ordered polar nanoregions (PNRs) [22–24]. PNRs form upon cooling from the high temperature cubic phase and eventually either freeze into a nonergodic state or transform into larger ferroelectric domains [22]. The absence of a long-range ferroelectric order and the presence of PNRs on the nanoscale length results in low-energy barriers for dipole reorientation [25]. $P4bm$ nanodomains are proposed to give rise to the nonergodic relaxor characteristics [17]. Here, the polarization can fluctuate around the six $\langle 001 \rangle_{\text{pc}}$ directions, enabling the pronounced frequency dispersion of permittivity [17]. The $P4bm$ phase is denoted as the relaxor phase [13], while the tetragonal nanodomains can be termed analogous to PNRs [26,27]. Neutron diffuse scattering experiments show diffuse streaking along $\langle 001 \rangle_{\text{pc}}$, revealing planar disk-shaped PNRs [28]. A direct correlation between the relaxor behavior and the evolution of such PNRs was drawn [27]. It is assumed that both $R3c$ and $P4bm$ PNRs coexist in the MPB compositions [20] and allow for an easy conversion between the symmetries due to a small energy difference [21].

How nanodomains (or PNRs) and long-range ferroelectric domains are correlated within a single grain is still an open question. Here, transmission electron microscopy (TEM) is used to shed light on the transition from a short-range ordered relaxor structure into a long-range domain morphology. The techniques of highly resolved high angle annular dark-field

^{*}Corresponding author: fetzter@geo.tu-darmstadt.de

(HAADF) imaging in scanning transmission electron microscopy (STEM), selected area electron diffraction (SAED), and dark-field (DF) imaging in TEM mode are deployed. The association of nanoscale polar areas and larger domains is visualized, reflecting a complex hierarchical structure.

II. EXPERIMENT

Three unpoled compositions with a BT content of 6, 9, and 12 mol % were investigated, termed NBT-6BT, NBT-9BT, and NBT-12BT, respectively. The ceramics were prepared via solid state synthesis route from Na_2CO_3 (99.5 %), BaCO_3 (99.8 %), Bi_2O_3 (99.975 %), and TiO_2 (99.6 %) powders (all Alfa Aesar, Kandel, Germany). The reactants were dried before stoichiometric weighing and then milled in ethanol for 24 h. Calcination of the dried powder was conducted at 900 °C for 3 h followed by a second milling step, sieving, and subsequent uniaxial isostatic pressing. The cylindrical green bodies were sintered at 1150 °C for 3 h with a heating rate of 5 °C/min. For electrical measurements, samples with a diameter of 11–12 mm were ground to 0.6 mm, annealed to relieve induced mechanical stresses and sputtered with Ag electrodes. The frequency-dependent permittivity was measured at ambient conditions on the unpoled, cylindrical samples using an impedance analyzer (Alpha-Analyzer, Novocontrol, Montabaur, Germany). TEM specimens were prepared by grinding and polishing a 3-mm-diameter disk down to 20 μm , successively annealing it at 400 °C, followed by thinning to perforation under an Ar^+ -ion beam in a DuoMill 600 (Gatan, Pleasanton, USA). The TEM experiments were carried out with a JEM-2100F microscope (JEOL, Tokyo, Japan), equipped with an energy-dispersive x-ray (EDS) detector (Oxford Instruments, Abingdon, UK). Zone axes of diffraction patterns were indexed corresponding to a pseudocubic structure with the help of a program for interpreting electron diffraction patterns [29]. High-resolution scanning transmission electron microscopy (HR-STEM) was carried out with a C_s -corrected JEM-ARM200F microscope (JEOL, Tokyo, Japan). To find the atom positions and map the corresponding polar displacement in the HAADF-STEM images, the Python-based programs ATOMAP [30] and TEMUL Toolkit [31] were used.

III. RESULTS AND DISCUSSION

The analyzed NBT-BT ceramics range from MPB (NBT-6BT), over near-MPB (NBT-9BT), to off-MPB (NBT-12BT) compositions. The EDS data illustrate that the Ba content within the compositions gradually increases (Fig. 1). NBT-6BT and -9BT display a similar relaxor behavior, indicated by the high permittivity ϵ' and pronounced frequency dispersion (Fig. 2). An elevated permittivity of relaxor materials is related to the high number of interfaces or domain wall density [32]. NBT-12BT shows less frequency dependence in permittivity due to a more ferroelectric nature, which is attributed to a larger domain size with a more narrow distribution [33,34].

The high permittivity of NBT-6BT can be linked to the short-range polar structures characterizing the relaxor composition. The terminology for nanometer-sized polar regions

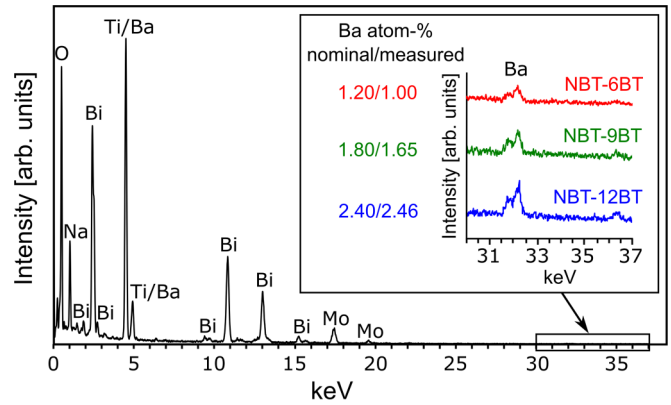


FIG. 1. EDS spectrum of a NBT-6BT grain obtained in the TEM (the Mo peak is due to the TEM grid material). The inset displays the Ba $K\alpha_1$ and $K\alpha_2$ peaks in the three compositions and the increasing nominal (stoichiometric) and measured Ba at. % values.

holds a certain ambiguity, often termed PNRs or nanodomains interchangeably. Here, we refer to atomic-scale fluctuations in the polar displacement as PNRs. The 1–4 nm large PNRs can be visualized using highly resolved HAADF-STEM imaging (Fig. 3). Bright regions imaged in TEM-DF, reflecting the symmetry based on oxygen octahedral tilting, are termed nanodomains (5–25 nm in size; compare Fig. 5). In contrast, regular ferroelectric domains can be up to the micrometer range in size [compare also Fig. 6(a)].

Figures 3(a)–3(c) illustrate short-ranged variations (PNRs) in the direction and magnitude of the polar displacement in NBT-6BT, viewed along the $[010]_{\text{pc}}$ zone axis. NBT and its solid solutions not only exhibit displacement of the B-site but also of the A-site atoms [6]. Here, the polar vectors [yellow arrows in Fig. 3(a)] indicate the relative Ti^{4+} displacement (B-site) with reference to the A-site sublattice. The position of the anions (O^{2-}) is not accounted for, since oxygen atoms are not visible in HAADF images. Regarding the $a^0a^0c^+$ tilt

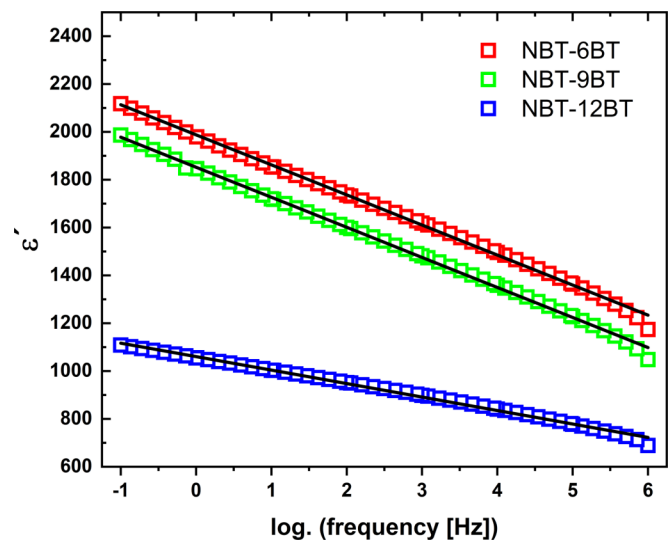


FIG. 2. Permittivity ϵ' of unpoled NBT-6BT, NBT-9BT, and NBT-12BT as a function of the logarithm of the measuring frequency. Linear fits are plotted as straight black lines.

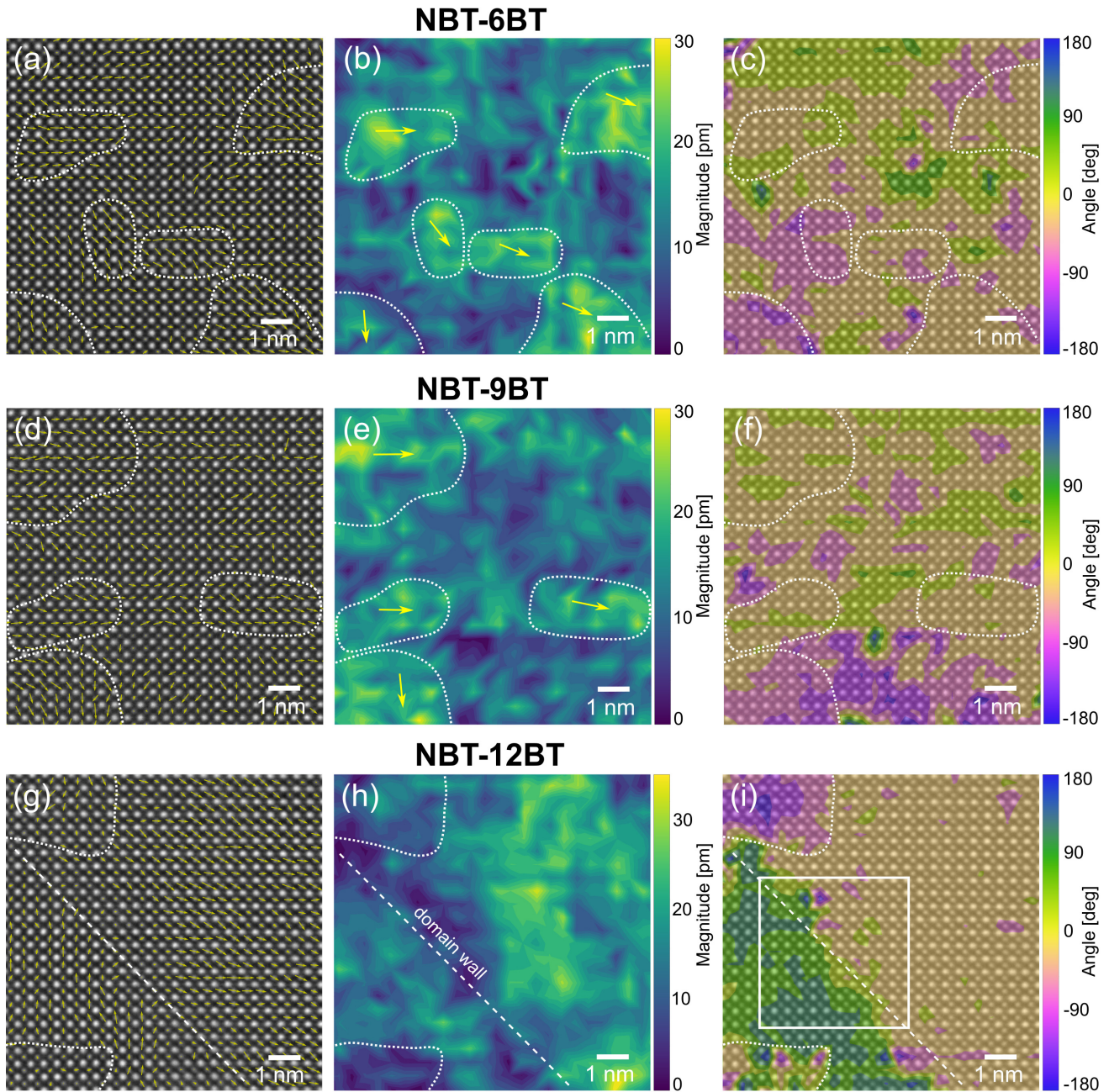


FIG. 3. High-resolution HAADF-STEM images of NBT-6BT, -9BT, and -12BT viewed along the $[010]_{pc}$ zone axis. Panel (a) depicts the polar displacement of Ti^{4+} with reference to the A site as yellow arrows in NBT-6BT. Panel (b) shows the magnitude of polar displacement. PNRs become visible, indicated by the dotted white lines. Panel (c) illustrates the direction of polar displacement as an angle color map. The same configuration applies for NBT-9BT in (d)–(f) and for NBT-12BT in (g)–(i). The square-shaped inset in (i) is magnified in Fig. 4(b).

system of $P4bm$, the oxygen octahedra are tilted around the c axis. Thus, when viewed along $\langle 010 \rangle_{pc}$, the plane in which the oxygen atoms are tilted either lies parallel or perpendicular to the viewing plane. This should not change the center of mass for the anions. The displayed polar vectors can thus be assumed to be very close to the real polarization direction. The polar vectors vary by approximately $\pm 90^\circ$ around an average direction [Fig. 3(c)]. Islandlike regions (dotted white lines) of few nanometers in size display a coherent and pronounced polar displacement. The magnitude of displacement within those PNRs is higher compared to the surrounding

[Fig. 3(b)]. The transition between the PNRs is gradual and significant areas with zero polar displacement are absent.

Mapping of the NBT-9BT composition [Figs. 3(d)–3(f)] displays similar features as described for NBT-6BT. The heterogeneous microstructure of the MPB and near-MPB compositions is in contrast to the more homogeneous and ordered structure in the off-MPB composition NBT-12BT. The polar displacement near a ferroelectric 90° domain wall is displayed in Figs. 3(g)–3(i). While the magnitude of polarization along the domain wall is reduced [Fig. 3(h)], a pronounced and coherent polar displacement is present within

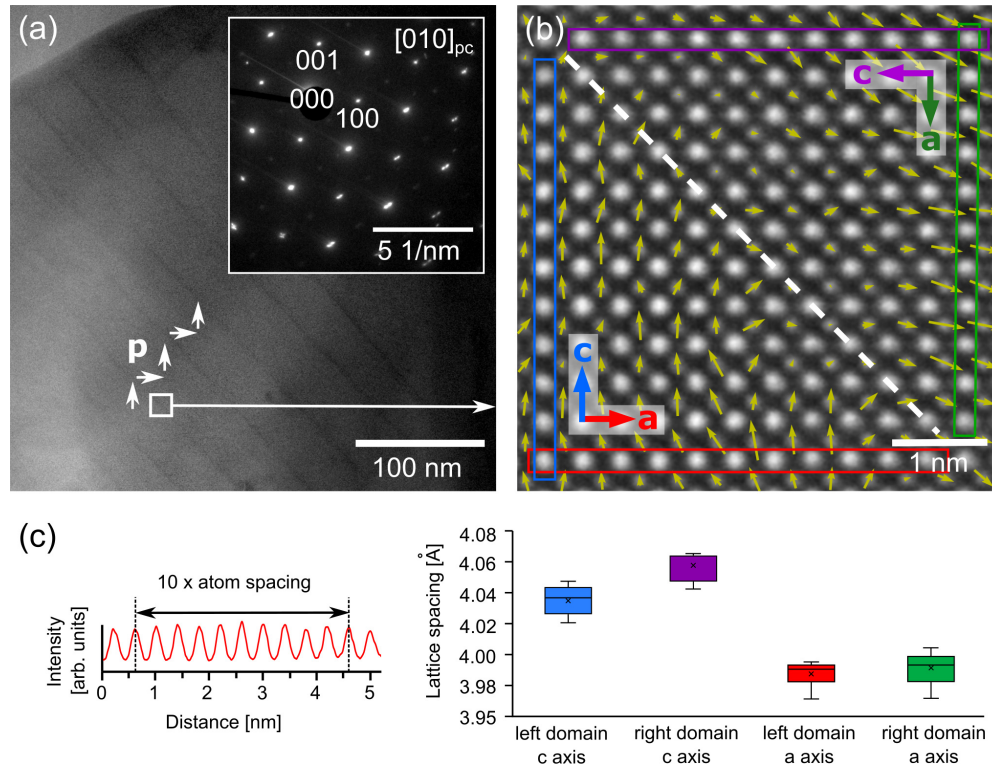


FIG. 4. (a) STEM bright field (BF) image of ferroelectric domains in NBT-12BT and corresponding SAED pattern. The 90° polarization “p” is indicated with arrows. (b) HAADF image of a domain wall [inset in Fig. 3(i)] and mapped polarization vectors (yellow arrows). Intensity profiles were drawn over ten atom spacings, indicated by the colored rectangles. (c) The plot on the left depicts an exemplary intensity profile. The plot on the right shows the lattice spacing along a and c axis on each side of the domain wall. Values were obtained from ten profiles each.

both domains [Fig. 3(g)]. However, local regions of a few nanometers in size display a divergence from the average polar direction [Fig. 3(i), dotted white lines]. These local areas reflect the presence of a reduced population of PNRs prevailing within the ferroelectric domains. The findings demonstrate a hierarchical microstructure where nanometer-sized polar regions and ferroelectric domains are closely associated. The weak frequency dispersion of permittivity noted for NBT-12BT (Fig. 2) can be rationalized by the coexistence of ferroelectric domains and relaxor-type PNRs.

Local variances in cationic displacement in NBT-BT is known to affect the local distortion and symmetry [35]. Bi^{3+} is found to exhibit a larger off-centering than Na^+ due to its lone pair character and orbital hybridization with oxygen [36]. A correlated displacement of Bi^{3+} is assumed to promote the formation of locally ordered PNRs [28]. The direction of Bi^{3+} displacement was found to change with increasing BT content [28]. The increase of Ba^{2+} on the A site in NBT-12BT and the consequential decrease in Bi^{3+} therefore relates to a reduced population of PNRs and favors a long-range ferroelectric structure.

HAADF-STEM imaging further allows us to determine lattice parameters in the lamellar ferroelectric $P4mm$ domains. In NBT-12BT, an alternating 90° polarization direction is present [Fig. 4(a)]. The polar vectors change from the $[001]_{pc}$ towards the $[100]_{pc}$ direction, when crossing the $(101)_{pc}$ domain wall. This observation also confirms the feasibility of the applied analysis technique. By measuring atomic distances [colored

line profiles in Fig. 4(b)], the lattice spacing can be calculated and correlated to the a and c crystal axis on each side of the domain wall [Fig. 4(c)]. The differences of a and c axes are in good agreement with lattice parameters obtained from high-resolution x-ray powder diffraction measurements on the same composition (see the Supplemental Material of Ref. [37]). The highly magnified image in Fig. 4(b) does not display PNRs in this specific local area, however, slight irregularities in both polarization directions are visible.

In order to further examine the local structural configurations, TEM-DF imaging acts as a viable tool to directly visualize the nanoscale morphology and association of different phases. The phase coexistence of T ($P4bm$) and R ($R3c$) symmetries in NBT-6BT has been demonstrated in previous TEM results [38,39]. Here, focus is laid on the $P4bm$ phase, since it constitutes the relaxor characteristic polar nanoregions. The bright-field (BF) image of a grain along the $[111]_{pc}$ zone axis [Fig. 5(a)] features a grainy contrast. Large domains are absent, indicating the nanoscale structure of $P4bm$. The corresponding SAED pattern in Fig. 5(b) depicts $\frac{1}{2}\{ooe\}$ SR. They can be divided into three different variants: $\frac{1}{2}(oeo)$, $\frac{1}{2}(eoo)$, and $\frac{1}{2}(ooe)$. Each variant is slightly elongated in one particular reciprocal direction [Fig. 5(c)]. DF imaging can be used to visualize the corresponding excited regions by selecting a SR with a small objective aperture. In Figs. 5(d)–5(f), the DF image of each variant is displayed. The SR is encircled in the SAED pattern in Fig. 5(c) with the corresponding color, respectively. Bright nanodomains of approximately

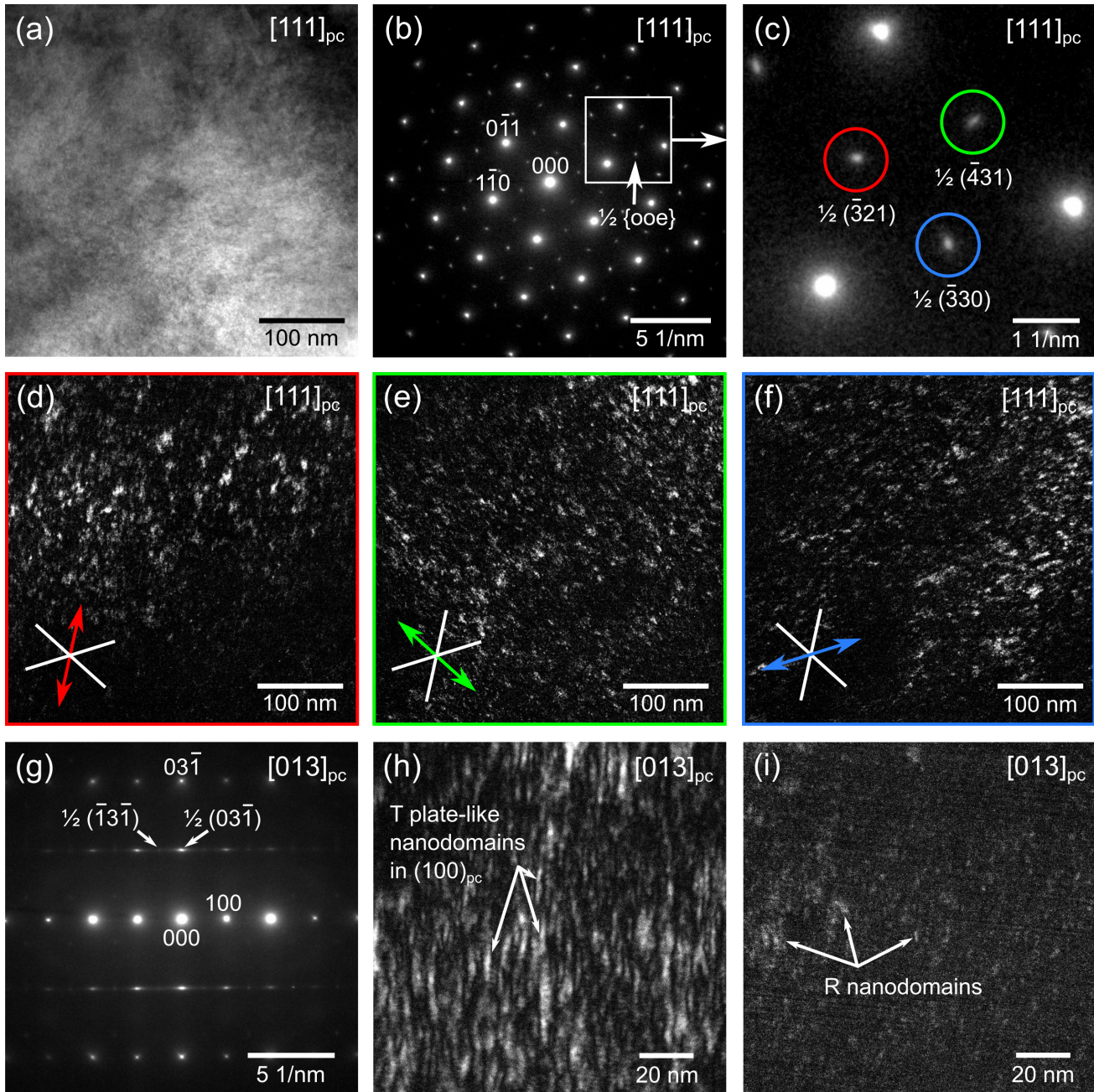


FIG. 5. TEM-BF image of a rather featureless grain in NBT-6BT (a), the corresponding SAED pattern (b), and an enlarged region highlighting the three variants of the $\frac{1}{2}\{ooo\}$ SR (c). The three marked reflections $\frac{1}{2}(321)$, $\frac{1}{2}(431)$, and $\frac{1}{2}(330)$ correspond to the three variants $\frac{1}{2}(oeo)$, $\frac{1}{2}(eoo)$, and $\frac{1}{2}(ooe)$, respectively. The DF images of the same area as in (a), obtained from the encircled SR in (c), are displayed in (d)–(f), featuring slightly elongated nanodomains. The elongation direction projected on the $(111)_{pc}$ viewing plane is emphasized by the red, green, and blue arrows, respectively. (g) SAED pattern in NBT-6BT viewed along the $[013]_{pc}$ zone axis, depicting elongated $\frac{1}{2}(eoo)$ SR and very weak $\frac{1}{2}(ooo)$ SR. Panel (h) shows the DF image of the $\frac{1}{2}(03\bar{1})$ SR and the platelike morphology of the $P4bm$ variant oriented in the $(100)_{pc}$ plane. (i) DF image of the very faint $\frac{1}{2}(\bar{1}3\bar{1})$ SR, revealing the presence of a minor amount of $R3c$ nanodomains.

5–25 nm become visible, displaying an elongated shape which is perpendicular to the elongation of the corresponding SR. The elongation direction projected on the viewing plane is indicated by the red, green, and blue arrows in Figs. 5(d)–5(f). In fact, the tetragonal c axis of each variant points towards one of the three main pseudocubic axes. This results in platelike nanodomains lying in $\{001\}_{pc}$ planes and SR stretch-

ing along $\langle 001 \rangle_{pc}$ directions [9,40]. Imaged along $[111]_{pc}$, the nanodomains are thus inclined towards the viewing direction. Their platelike character becomes well visible when imaged along the $[013]_{pc}$ zone axis. Here, the viewing direction is parallel to the $(100)_{pc}$ plane. The $\frac{1}{2}(eoo)$ SR stretches along the $[100]_{pc}$ direction in the SAED pattern [Fig. 5(g)]. The corresponding DF image [Fig. 5(h)] illustrates the platelike

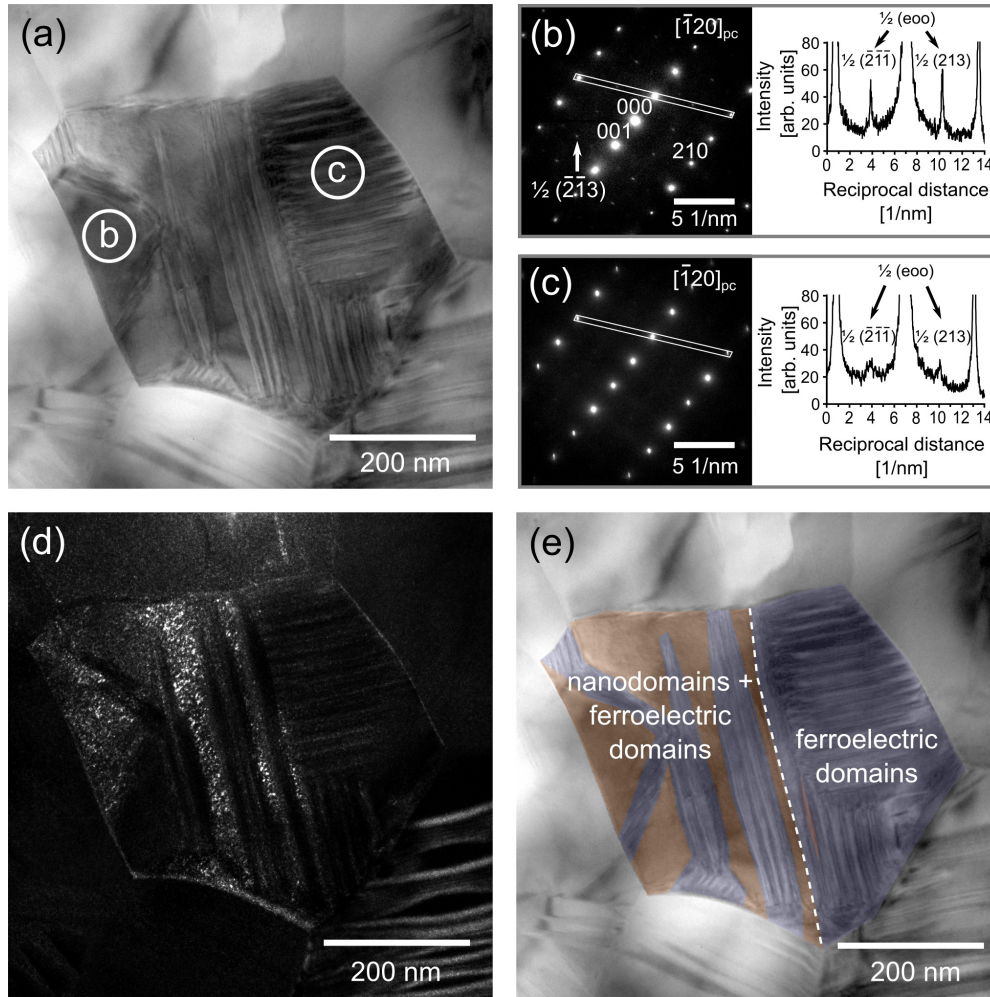


FIG. 6. (a) TEM-BF image of a grain in NBT-9BT, where (b) and (c) display SAED patterns of regions marked in (a). Corresponding intensity profiles are drawn over the main and superlattice reflections. (d) DF image obtained from a $\frac{1}{2}(e00)$ SR, namely the $\frac{1}{2}(\bar{2}\bar{1}3)$ reflection, depicting the location of $P4bm$ nanodomains. (e) Color map of nanodomains (orange) and long-range ferroelectric domains (blue).

nanodomains lying in the $(100)_{pc}$ plane. Taking a closer look at the SAED pattern [Fig. 5(g)], very faint $\frac{1}{2}(000)$ SR can be observed as well, indicating the presence of a minor amount of the $R3c$ phase. The corresponding DF image [Fig. 5(i)] reveals rhombohedral nanodomains up to 20 nm in size located between the T nanodomains.

It has been hypothesized that the dark matrix consists of other tetragonal variants and a cubic phase [17,41]. However, models for the nanoscale structure of relaxors are controversial. The concept of PNRs embedded within a nonpolar matrix is widely adopted. The concept of ferroelectric nanodomains, which are separated by a high density of domains walls, makes the presence of a cubic matrix obsolete. The latter serves as a more suited model fitting experimental observations such as diffuse scattering experiments [42]. For classical relaxors such as $\text{Pb}(\text{Mg}_{1/3}\text{Nb}_{2/3})\text{O}_3$ (PMN)-based materials, a continuously and smoothly varying polar displacement across nanoregion boundaries could be demonstrated [43]. A multidomain state with domains of very few nanometers in size was simulated, invalidating the existence of a nonpolar matrix [44]. From the DF images in Fig. 5 it can be concluded that the volume of NBT-6BT is primarily built up by densely packed variants

of platelike T nanodomains and a minor volume fraction of antiphase tilted R nanodomains. These findings agree with the modeled oxygen octahedral tilt disorder in NBT-5BT, where T platelike regions are surrounded by R nanodomains [45]. From the TEM observations in this study, it cannot be established with certainty if a nonpolar cubic matrix is present.

NBT-9BT marks a transition between the relaxor and ferroelectric states. The predominantly tetragonal composition exhibits relaxor behavior, as illustrated by the strong frequency dependence of permittivity (Fig. 2). The microstructure already comprises a high fraction of long-range lamellar $P4mm$ domains [37]. Figure 6(a) displays a grain in NBT-9BT, where the right half is fully occupied by lamellar domains. The left half features intergrowth of domain bands and regions, revealing no pronounced contrast. The latter correspond to the heterogeneous area imaged in Figs. 3(d)–3(f). A SAED pattern from the region without domains [Fig. 6(b)] exhibits well visible $\frac{1}{2}(e00)$ SR, while the SAED pattern of the lamellar domains [Fig. 6(c)] does not show any obvious SR. However, the intensity profile reveals small SR remnants. They are not completely absent, but only of very weak intensity. The DF image of the $\frac{1}{2}(\bar{2}\bar{1}3)$ SR [Fig. 6(d)]

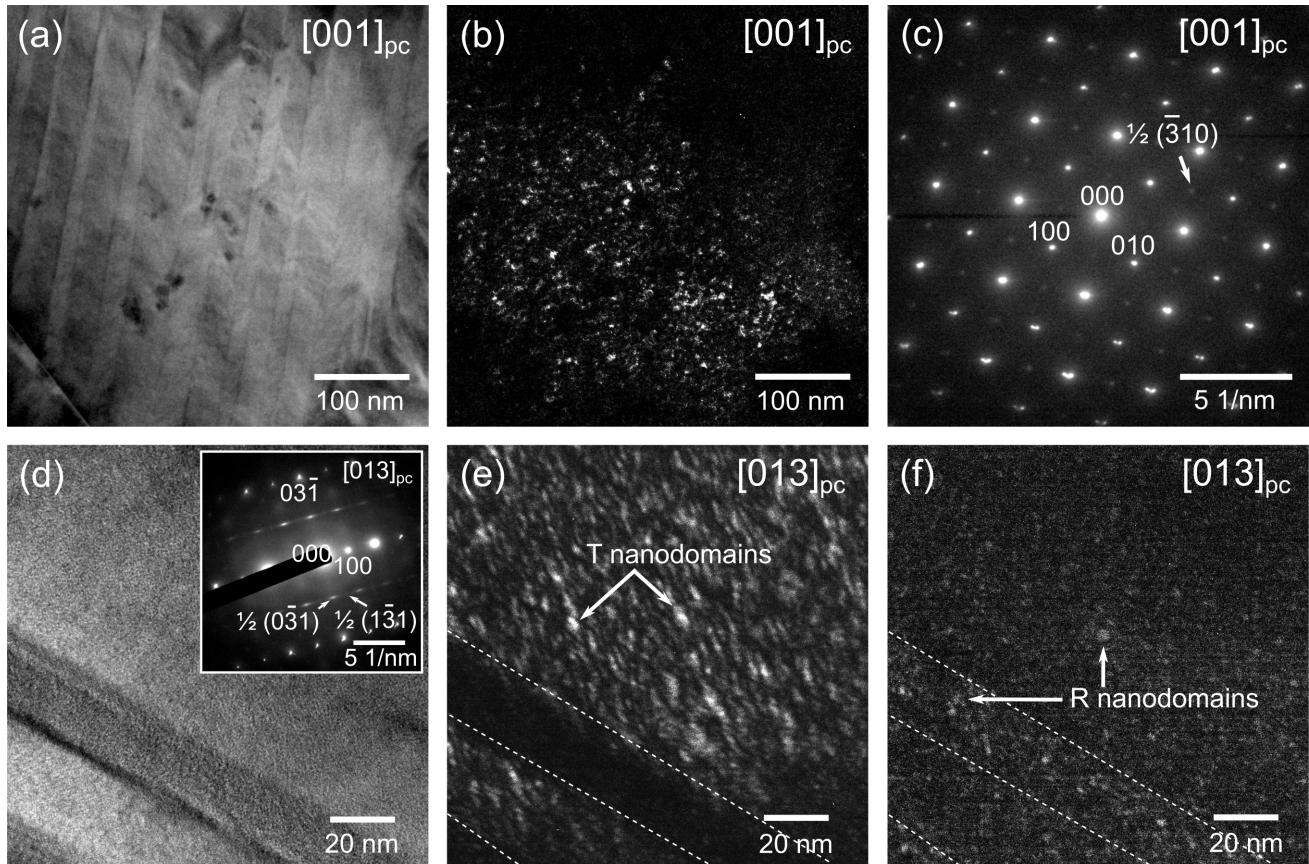


FIG. 7. (a) TEM-BF micrograph of lamellar domains in NBT-12BT viewed along the $[001]_{pc}$ zone axis. (b) Corresponding DF image obtained from the marked $\frac{1}{2}(ooe)$ SR [the $\frac{1}{2}(\bar{3}10)$ reflection] in (c), clearly revealing the presence of $P4bm$ nanodomains embedded within the lamellar domains. (d) BF image of another grain in NBT-12BT viewed along the $[013]_{pc}$ zone axis and corresponding SAED pattern. Panels (e) and (f) show the DF images obtained from the marked $\frac{1}{2}(0\bar{3}1)$ and $\frac{1}{2}(1\bar{3}1)$ SR, respectively. Both T and R nanodomains are present.

illustrates the location of the $P4bm$ nanodomains. Figure 6(e) visualizes the intergrowth of nanodomain-dominated areas (orange) and ferroelectric domains (blue). The $P4mm$ symmetry does not feature tilting of oxygen octahedra. However, a very weak nanodomain signal also arises from within the ferroelectric domains [Fig. 6(d)]. Their population within the ferroelectric domains appears significantly reduced.

In the ferroelectric NBT-12BT specimen, which features pronounced lamellar $P4mm$ domains, very weak $\frac{1}{2}\{ooe\}$ SR can still be observed. The occurrence of a small $P4bm$ fraction results in an overall less ordered ferroelectric structure. These characteristics are illustrated in Figs. 7(a)–7(c). The grain features a ferroelectric domain contrast with a lamellar $(1\bar{1}0)_{pc}$ domain wall configuration [Fig. 7(a)]. The corresponding DF image [Fig. 7(b)] obtained from the marked $\frac{1}{2}(ooe)$ SR [Fig. 7(c)] clearly reveals the presence of $P4bm$ nanodomains embedded within the lamellar domains. These findings add a further complexity to the ferroelectric structure, which however cannot be inferred from BF imaging alone. When viewed along the $[013]_{pc}$ zone axis [Figs. 7(d)–7(f)], the platelike character of the T nanodomains is still preserved. However, compared to NBT-6BT in Fig. 5(h), they are slightly reduced in size (now 3–15 nm). Interestingly, the T nanodomains are absent from a domain band marked in Fig. 7(e) by the dashed white lines. This is an indication that within the lamellar

domains, not all three variants of the $P4bm$ nanodomains occur. Unexpectedly, nanodomains of $R3c$ symmetry occurring within the lamellar domains could be detected in NBT-12BT as well [Fig. 7(f)]. Thus, local rhombohedral antiphase tilted regions still prevail in compositions with such a high BT content.

A summarizing schematic [Fig. 8(a)] illustrates the compositionally induced transition from the relaxor structure at the MPB towards a ferroelectric domain morphology. The latter still entails $T + R$ nanodomains in a reduced population. For pure NBT, the occurrence of tetragonal platelets within lamellar $R3c$ domains was reported [9], which correlates with the hierarchical structure in BT-rich compositions. It has to be further noted that a very small macroscopic rhombohedral volume fraction also prevails in the NBT-9BT and -12BT compositions.

The HAADF images revealed a heterogeneous local structure in the relaxor compositions (compare Fig. 3). Variations in the polar displacement, denoted as PNRs, are present on an atomic level. The size of these PNRs (1–4 nm) only spans several unit cells, while the $P4bm$ nanodomains can be up to 25 nm in size. This suggests that the local fluctuations imaged in Figs. 3(a)–3(f) occur within a $P4bm$ nanodomain variant. It can be inferred that T nanodomains can be built up by PNRs featuring a superordinate polarization direction, which

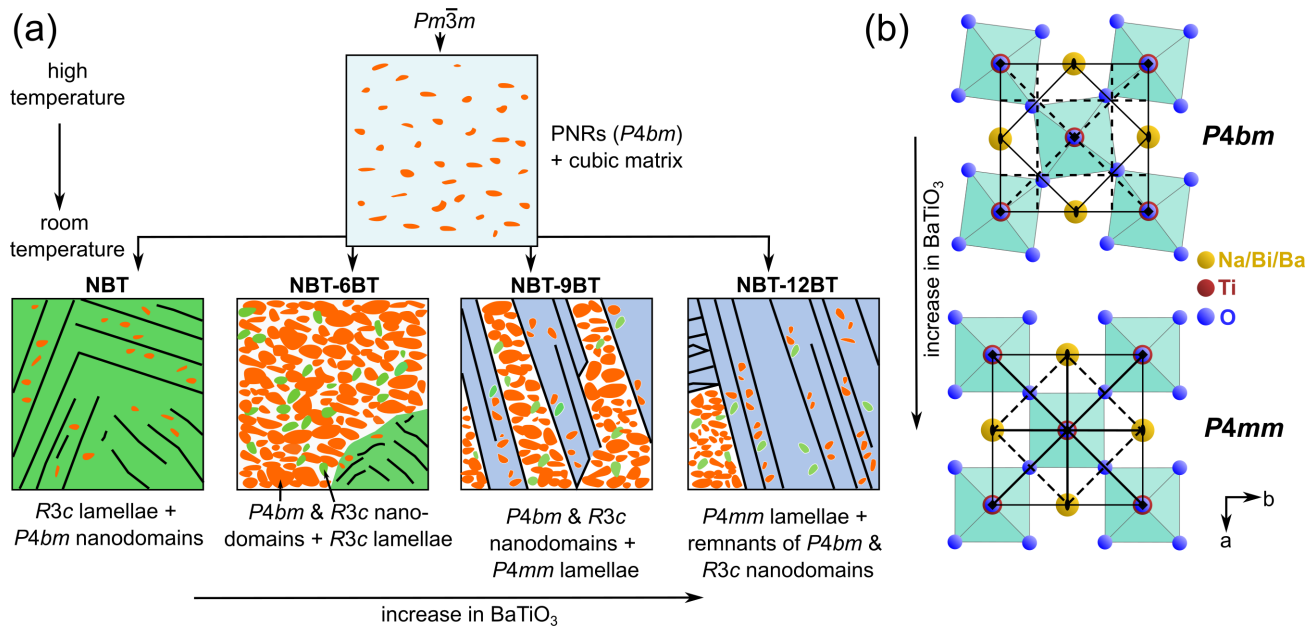


FIG. 8. (a) Schematic describing the structural changes in the NBT-BT system with increasing BT content, emphasizing the hierarchical microstructural development. The structure of pure NBT is based on the description by Dorcet and Trolliard [9]. (b) Crystal structure and according symmetry operations (solid lines = mirror planes vs dashed lines = glide planes) of the $P4bm$ phase, where $a^0a^0c^+$ tilting of oxygen octahedra is present and the $P4mm$ phase, where tilting is absent.

corresponds to the [001] direction of the variant. The polar vector can thus fluctuate around an average direction within the nanodomains, promoting the monitored relaxational behavior.

The presence of both $P4bm$ and $R3c$ polar regions in NBT-6BT was previously inferred from the occurrence of both types of SR [21]. The DF images (Fig. 5) now provide visual evidence that the bulk of NBT-6BT is indeed built up by dispersed $P4bm$ and $R3c$ nanometer-sized domains. Low energy barriers between both symmetries can enable an easy polarization reversal. Therefore, it can be assumed that a facilitated transformation of $P4bm$ and $R3c$ PNRs promotes the relaxor behavior reflected in the temperature dependent frequency dispersion of permittivity [21].

Although the ferroelectric domains in NBT-12BT display on average a consistency in polarization direction and magnitude, nanoscale areas of incoherent polar displacement occur [compare Figs. 3(g)–3(i)]. This is corroborated by the presence of T and R nanodomains within the ferroelectric domains, as verified by DF imaging (Fig. 7). The observations validate that the coexistence of all three phases ($P4mm + P4bm + R3c$) spans over a wide compositional range. Complex domain arrangements are also reported for the relaxor ferroelectric $\text{Pb}(\text{Mg}_{1/3}\text{Nb}_{2/3})\text{O}_3\text{-PbTiO}_3$ (PMN-PT). Monoclinic and MPB compositions feature microscale domains with striationlike nanodomains, which, unlike here, disappear in the tetragonal $P4mm$ phase [46]. It could, however, be demonstrated on relaxor-PT solid solutions that PNRs within a ferroelectric matrix can enable an easy polarization rotation during poling and thus significantly contribute to the high piezoelectricity of relaxor-ferroelectric materials [47].

The formation of a ferroelectric long-range order (by changing the BT content or by poling) has been related to an increase in size and coherence length of polar nanoscale

regions [41]. The findings here, however, illustrate that the nanodomains do not grow and coalesce into larger structures. Instead, a reduction in size by up to 10 nm was observed in NBT-12BT. The transformation can rather be viewed analogous to a recrystallization process, where the $P4bm$ nanodomains undergo a transition to a $P4mm$ symmetry. Nanodomains, in which the polar axis is in favor of the average ferroelectric polarization within the $P4mm$ domain, may transform more easily. This can reduce the number of variants within the domains from three to two or even one. When comparing both tetragonal phases, the difference in symmetry arises by the $a^0a^0c^+$ in-phase tilting of oxygen octahedra in the $P4bm$ phase, which causes the appearance of mirror glide planes compared to $P4mm$ [Fig. 8(b)]. In general, tilting of oxygen octahedra enables a larger flexibility in the coordination of the A site [48]. In NBT-BT, the A site is occupied by Na^+ , Bi^{3+} , and Ba^{2+} cations. Since Na^+ and Bi^{3+} have relatively small ionic radii, octahedral tilting in pure NBT is expected [6]. Tilting reduces the volume of the intermediate space of the A site and therefore supports the stability of the structure [49]. Ba^{2+} on the other hand has a larger ionic radius, so that oxygen octahedra are not tilted in pure BT. By increasing the percentage of Ba^{2+} cations on the A site, oxygen octahedral tilting is continuously reduced and finally absent, accounting for the transition towards $P4mm$. The partial persistence of nanodomains can be rationalized by very local chemical heterogeneities, locally allowing tilting of oxygen octahedra. Due to the reduced free space on the A site by the Ba^{2+} increase, an overall reduction in cationic displacement can be expected [50]. Likewise, off-centering of the Bi^{3+} cations, which promotes the relaxational behavior, is reduced with increasing BT content. However, it clearly needs to be considered that a certain degree of tilt disorder, evidenced by both T and R nanodomains, is still present

in BT-rich compositions. This is further corroborated by the reduced, however still existing, frequency dispersion of the permittivity in the NBT-12BT sample.

IV. CONCLUSIONS

In unpoled NBT-BT ceramics, HAADF-STEM and TEM-DF imaging act as viable tools to portray the correlation of short-range polar structures (nanodomains and PNRs) and large ferroelectric domains. Both are inherent to the relaxor-ferroelectric system. The techniques are used to visualize the evolution from a nanoscale relaxor structure towards an association of nano- and ferroelectric domains with increasing BT content. The major volume fraction at the MPB (NBT-6BT) is characterized by three variants of platelike $P4bm$ nanodomains, dispersed with a minor fraction of $R3c$ nanodomains. Short-ranged variances (PNRs) in the direction and magnitude of the polar displacement occurring within a variant underpin the heterogeneous structure. The nanoscale structural fluctuations and coexisting phases can facilitate polarization reversal, which accounts for the relaxor-typical

enhanced piezoelectric response and high permittivity. Inter-growth of lamellar $P4mm$ domains and nanodomains occurs with increasing BT content (NBT-9BT). It should be emphasized that the nanodomains do not coalesce into larger polar structures. Instead, the structural transition towards an overall $P4mm$ symmetry is associated with the increase of Ba^{2+} on the A-cation site and, as a consequence, an overall reduction in oxygen octahedral tilting. However, small volume fractions of $P4bm$ and $R3c$ nanodomains still remain embedded within the ferroelectric domains even at a higher BT content (NBT-12BT). A hierarchical and complex arrangement of short-range and long-range polar structures results. The observed hierarchical association demonstrates that the microstructure itself clearly differentiates from a typical well-ordered ferroelectric material.

ACKNOWLEDGMENTS

The financial support by the Deutsche Forschungsgemeinschaft (DFG, German Research Foundation) under KL 615/34-1 and KO 5948/1-1 (Grant No. 414311761) is gratefully acknowledged.

-
- [1] K. Uchino, Relaxor ferroelectric-based ceramics, in *Advanced Piezoelectric Materials*, 2nd ed. (Woodhead Publishing, Sawston, UK, 2017), pp. 127–153.
 - [2] T. Tou, Y. Hamaguti, Y. Maida, H. Yamamori, K. Takahashi, and Y. Terashima, Properties of $(Bi_{0.5}Na_{0.5})TiO_3$ - $BaTiO_3$ - $(Bi_{0.5}Na_{0.5})(Mn_{1/3}Nb_{2/3})O_3$ lead-free piezoelectric ceramics and its application to ultrasonic cleaner, *Jpn. J. Appl. Phys.* **48**, 07GM03 (2009).
 - [3] Y. Doshida, H. Shimizu, Y. Mizuno, and H. Tamura, Investigation of high-power properties of $(Bi, Na, Ba)TiO_3$ and $(Sr, Ca)_2NaNb_5O_{15}$ piezoelectric ceramics, *Jpn. J. Appl. Phys.* **52**, 07HE01 (2013).
 - [4] M. Slabki, L. Kodumudi Venkataraman, T. Rojac, J. Rödel, and J. Koruza, Thermal stability of the electromechanical properties in acceptor-doped and composite-hardened $(Na_{1/2}Bi_{1/2})TiO_3$ - $BaTiO_3$ ferroelectrics, *J. Appl. Phys.* **130**, 014101 (2021).
 - [5] A. R. Paterson, H. Nagata, X. Tan, J. E. Daniels, M. Hinterstein, R. Ranjan, P. B. Groszewicz, W. Jo, and J. L. Jones, Relaxor-ferroelectric transitions: Sodium bismuth titanate derivatives, *MRS Bull.* **43**, 600 (2018).
 - [6] G. O. Jones and P. A. Thomans, Investigation of the structure and phase transitions in the novel A-site substituted distorted perovskite compound $Na_{0.5}Bi_{0.5}TiO_3$, *Acta Crystallogr., Sect. B* **58**, 168 (2002).
 - [7] E. Aksel, J. S. Forrester, J. L. Jones, P. A. Thomas, K. Page, and M. R. Suchomel, Monoclinic crystal structure of polycrystalline $Na_{0.5}Bi_{0.5}TiO_3$, *Appl. Phys. Lett.* **98**, 152901 (2011).
 - [8] B. N. Rao, A. N. Fitch, and R. Ranjan, Ferroelectric-ferroelectric phase coexistence in $Na_{1/2}Bi_{1/2}TiO_3$, *Phys. Rev. B* **87**, 060102 (2013).
 - [9] V. Dorcet and G. Trolliard, A transmission electron microscopy study of the A-site disordered perovskite $Na_{0.5}Bi_{0.5}TiO_3$, *Acta Mater.* **56**, 1753 (2008).
 - [10] R. H. Buttner and E. N. Maslen, Structural parameters and electron difference density in $BaTiO_3$, *Acta Crystallogr., Sect. B* **48**, 764 (1992).
 - [11] G. Arlt and P. Sasko, Domain configuration and equilibrium size of domains in $BaTiO_3$ ceramics, *J. Appl. Phys.* **51**, 4956 (1980).
 - [12] C. Ma, H. Guo, S. P. Beckman, and X. Tan, Creation and Destruction of Morphotropic Phase Boundaries Through Electrical Poling: A Case Study of Lead-Free $(Bi_{1/2}Na_{1/2})TiO_3$ - $BaTiO_3$ Piezoelectrics, *Phys. Rev. Lett.* **109**, 107602 (2012).
 - [13] G. D. Adhikary, B. Mahale, B. N. Rao, A. Senyshyn, and R. Ranjan, Depoling phenomena in $Na_{0.5}Bi_{0.5}TiO_3$ - $BaTiO_3$: A structural perspective, *Phys. Rev. B* **103**, 184106 (2021).
 - [14] T. Takenaka, K. Maruyama, and K. Sakata, $(Bi_{1/2}Na_{1/2})TiO_3$ - $BaTiO_3$ system of lead-free piezoelectric ceramics, *Jpn. J. Appl. Phys.* **30**, 2236 (1991).
 - [15] C. Ma and X. Tan, Phase diagram of unpoled lead-free $(1-x)(Bi_{1/2}Na_{1/2})TiO_3$ - $xBaTiO_3$ ceramics, *Solid State Commun.* **150**, 1497 (2010).
 - [16] L. A. Schmitt, J. Kling, M. Hinterstein, M. Hoelzel, W. Jo, H.-J. Kleebe, and H. Fuess, Structural investigations on lead-free $Bi_{1/2}Na_{1/2}TiO_3$ -based piezoceramics, *J. Mater. Sci.* **46**, 4368 (2011).
 - [17] C. Ma, X. Tan, E. Dul'kin, and M. Roth, Domain structure-dielectric property relationship in lead-free $(1-x)(Bi_{1/2}Na_{1/2})TiO_3$ - $xBaTiO_3$ ceramics, *J. Appl. Phys.* **108**, 104105 (2010).
 - [18] R. Garg, B. N. Rao, A. Senyshyn, P. S. R. Krishna, and R. Ranjan, Lead-free piezoelectric system $(Na_{0.5}Bi_{0.5})TiO_3$ - $BaTiO_3$: Equilibrium structures and irreversible structural transformations driven by electric field and mechanical impact, *Phys. Rev. B* **88**, 014103 (2013).
 - [19] A. Wohninsland, A.-K. Fetzer, R. Broughton, J. L. Jones, and K. V. Lalitha, Structural and microstructural description of relaxor-

- ferroelectric transition in quenched $\text{Na}_{1/2}\text{Bi}_{1/2}\text{TiO}_3\text{-BaTiO}_3$, *J. Materiomics* (2022), doi: 10.1016/j.jmat.2022.01.006.
- [20] W. Jo, J. E. Daniels, J. L. Jones, X. Tan, P. A. Thomas, D. Damjanovic, and J. Rödel, Evolving morphotropic phase boundary in lead-free $(\text{Bi}_{1/2}\text{Na}_{1/2})\text{TiO}_3\text{-BaTiO}_3$ piezoceramics, *J. Appl. Phys.* **109**, 014110 (2011).
- [21] W. Jo, S. Schaab, E. Sapper, L. A. Schmitt, H.-J. Kleebe, A. J. Bell, and J. Rödel, On the phase identity and its thermal evolution of lead free $(\text{Bi}_{1/2}\text{Na}_{1/2})\text{TiO}_3\text{-6 mol% BaTiO}_3$, *J. Appl. Phys.* **110**, 074106 (2011).
- [22] A. A. Bokov, B. J. Rodriguez, X. Zhao, J.-H. Ko, S. Jesse, X. Long, W. Qu, T. H. Kim, J. D. Budai, A. N. Morozovska *et al.*, Compositional disorder, polar nanoregions and dipole dynamics in $\text{Pb}(\text{Mg}_{1/3}\text{Nb}_{2/3})\text{O}_3$ -based relaxor ferroelectrics, *Z. Kristallogr.* **226**, 99 (2011).
- [23] A. A. Bokov and Z.-G. Ye, Dielectric relaxation in relaxor ferroelectrics, *J. Adv. Dielectr.* **2**, 1241010 (2012).
- [24] R. A. Cowley, S. N. Gvasaliya, S. G. Lushnikov, B. Roessli, and G. M. Rotaru, Relaxing with relaxors: A review of relaxor ferroelectrics, *Adv. Phys.* **60**, 229 (2011).
- [25] C.-S. Chen, P.-Y. Chen, and C.-S. Tu, Polar nanoregions and dielectric properties in high-strain lead-free $0.93(\text{Bi}_{1/2}\text{Na}_{1/2})\text{TiO}_3\text{-0.07BaTiO}_3$ piezoelectric single crystals, *J. Appl. Phys.* **115**, 014105 (2014).
- [26] F. Craciun, C. Galassi, and R. Birjega, Electric-field-induced and spontaneous relaxor-ferroelectric phase transitions in $(\text{Na}_{1/2}\text{Bi}_{1/2})_{1-x}\text{Ba}_x\text{TiO}_3$, *J. Appl. Phys.* **112**, 124106 (2012).
- [27] W. Ge, C. Luo, C. P. Devreugd, Q. Zhang, Y. Ren, J. Li, H. Luo, and D. Viehland, Direct evidence of correlations between relaxor behavior and polar nano-regions in relaxor ferroelectrics: a case study of lead-free piezoelectrics $\text{Na}_{0.5}\text{Bi}_{0.5}\text{TiO}_3\text{-}x\%\text{BaTiO}_3$, *Appl. Phys. Lett.* **103**, 241914 (2013).
- [28] H. Zhang, G. Deng, A. J. Studer, X. Li, X. Zhao, and H. Luo, Neutron diffuse scattering of $(1-x)(\text{Na}_{0.5}\text{Bi}_{0.5})\text{TiO}_3\text{-}x\text{BaTiO}_3$ relaxor ferroelectric single crystals, *Scr. Mater.* **86**, 5 (2014).
- [29] G. Mieke, Program for Interpreting Electron Diffraction Patterns (PIEP), Version 7.12 (Department of Materials Science, Technical University of Darmstadt, 2002).
- [30] M. Nord, P. E. Vullum, I. MacLaren, T. Tybell, and R. Holmestad, Atomap: A new software tool for the automated analysis of atomic resolution images using two-dimensional gaussian fitting, *Adv. Struct. Chem. Imag.* **3**, 9 (2017).
- [31] E. O'Connell, TEMUL Toolkit, <https://temul-toolkit.readthedocs.io/en/latest/>, 2020.
- [32] V. V. Shvartsman, D. C. Lupascu, and D. J. Green, Lead-Free relaxor ferroelectrics, *J. Am. Ceram. Soc.* **95**, 1 (2012).
- [33] M. I. Morozov and D. Damjanovic, Charge migration in $\text{Pb}(\text{Zr}, \text{Ti})\text{O}_3$ ceramics and its relation to ageing, hardening, and softening, *J. Appl. Phys.* **107**, 034106 (2010).
- [34] D. V. Taylor and D. Damjanovic, Evidence of domain wall contribution to the dielectric permittivity in PZT thin films at sub-switching fields, *J. Appl. Phys.* **82**, 1973 (1997).
- [35] D. Maurya, M. Murayama, A. Pramanick, W. T. Reynolds, K. An, and S. Priya, Origin of high piezoelectric response in A-site disordered morphotropic phase boundary composition of lead-free piezoelectric $0.93(\text{Na}_{0.5}\text{Bi}_{0.5})\text{TiO}_3\text{-0.07BaTiO}_3$, *J. Appl. Phys.* **113**, 114101 (2013).
- [36] C. Moriyoshi, S. Takeda, Y. Kuroiwa, and M. Goto, Off-centering of a bi ion in cubic phase of $(\text{Bi}_{1/2}\text{Na}_{1/2})\text{TiO}_3$, *Jpn. J. Appl. Phys.* **53**, 09PD02 (2014).
- [37] A.-K. Fetzer, A. Wohninsland, K. Hofmann, O. Clemens, L. Kodumudi Venkataraman, and H.-J. Kleebe, Domain structure and phase evolution in quenched and furnace cooled lead-free $\text{Na}_{1/2}\text{Bi}_{1/2}\text{TiO}_3\text{-BaTiO}_3$ ceramics, *Open Ceram.* **5**, 100077 (2021).
- [38] A.-K. Fetzer, A. Wohninsland, K. V. Lalitha, and H. J. Kleebe, In situ hot-stage TEM of the phase and domain evolution in quenched $\text{Na}_{1/2}\text{Bi}_{1/2}\text{TiO}_3\text{-BaTiO}_3$, *J. Am. Ceram. Soc.* **105**, 2878 (2021).
- [39] C. Ma and X. Tan, *In situ* transmission electron microscopy study on the phase transitions in lead-free $(1-x)(\text{Bi}_{1/2}\text{Na}_{1/2})\text{TiO}_3\text{-}x\text{BaTiO}_3$ ceramics, *J. Am. Ceram. Soc.* **94**, 4040 (2011).
- [40] I. Levin and I. M. Reaney, Nano- and Mesoscale structure of $\text{Na}_{1/2}\text{Bi}_{1/2}\text{TiO}_3$: a TEM perspective, *Adv. Funct. Mater.* **22**, 3445 (2012).
- [41] P. B. Groszewicz, H. Breitzke, R. Dittmer, E. Sapper, W. Jo, G. Buntkowsky, and J. Rödel, Nanoscale phase quantification in lead-free $(\text{Bi}_{1/2}\text{Na}_{1/2})\text{TiO}_3\text{-BaTiO}_3$ relaxor ferroelectrics by means of ^{23}Na NMR, *Phys. Rev. B* **90**, 220104 (2014).
- [42] J. Hlinka, Do we need the ether of polar Nanoregions? *J. Adv. Dielectr.* **2**, 1241006 (2012).
- [43] M. Eremenko, V. Krayzman, A. Bosak, H. Y. Playford, K. W. Chapman, J. C. Woicik, B. Ravel, and I. Levin, Local atomic order and hierarchical polar nanoregions in a classical relaxor ferroelectric, *Nat. Commun.* **10**, 2728 (2019).
- [44] H. Takenaka, I. Grinberg, S. Liu, and A. M. Rappe, Slush-like polar structures in single-crystal relaxors, *Nature (London)* **546**, 391 (2017).
- [45] A. Neagu and C.-W. Tai, Investigation of local structural phase transitions in $95\text{Na}_{0.5}\text{Bi}_{0.5}\text{TiO}_3\text{-5BaTiO}_3$ piezoceramics by means of in-situ transmission electron microscopy, *J. Appl. Phys.* **123**, 244105 (2018).
- [46] M. Otoničar, A. Bradeško, L. Fulanović, T. Kos, H. Uršič, A. Benčan, M. J. Cabral, A. Henriques, J. L. Jones, L. Riemer *et al.*, Connecting the multiscale structure with macroscopic response of relaxor ferroelectrics, *Adv. Funct. Mater.* **30**, 2006823 (2020).
- [47] F. Li, S. Zhang, T. Yang, Z. Xu, N. Zhang, G. Liu, J. Wang, J. Wang, Z. Cheng, Z. G. Ye *et al.*, The origin of ultrahigh piezoelectricity in relaxor-ferroelectric solid solution crystals, *Nat. Commun.* **7**, 13807 (2016).
- [48] C. J. Howard, Structures and phase transitions in perovskites - a group-theoretical approach, *Acta Crystallogr., Sect. A* **61**, 93 (2005).
- [49] D. I. Woodward and I. M. Reaney, Electron diffraction of tilted perovskites, *Acta Crystallogr., Sect. B* **61**, 387 (2005).
- [50] S. R. Kanuru, K. Baskar, and R. Dhanasekaran, Synthesis, structural, morphological and electrical properties of NBT-BT ceramics for piezoelectric applications, *Ceram. Int.* **42**, 6054 (2016).